

A *Chandra* Study of the Lobe/ISM Interactions Around the Inner Radio Lobes of Centaurus A: Constraints on the Temperature Structure and Transport Processes

R. P. Kraft, P. E. J. Nulsen

Harvard/Smithsonian Center for Astrophysics, 60 Garden St., MS-67, Cambridge, MA 02138

M. Birkinshaw, D. M. Worrall

University of Bristol, Department of Physics, Tyndall Avenue, Bristol BS8 1TL, UK

R. F. Penna

*Harvard/Smithsonian Center for Astrophysics, 60 Garden St., Cambridge, MA 02138 and
Department of Physics and Astronomy, University of Rochester, 500 Wilson Boulevard,
Rochester, NY 14627*

W. R. Forman

Harvard/Smithsonian Center for Astrophysics, 60 Garden St., Cambridge, MA 02138

M. J. Hardcastle

*University of Hertfordshire, School of Physics, Astronomy, and Mathematics, Hatfield
AL10 9AB, UK*

C. Jones

Harvard/Smithsonian Center for Astrophysics, 60 Garden St., Cambridge, MA 02138

S. S. Murray

Harvard/Smithsonian Center for Astrophysics, 60 Garden St., Cambridge, MA 02138

ABSTRACT

We present results from deeper *Chandra* observations of the southwest radio lobe of Centaurus A, first described by Kraft *et al.* (2003). We find that the sharp X-ray surface brightness discontinuity extends around $\sim 75\%$ of the periphery of the radio lobe, and detect significant temperature jumps in the brightest

regions of this discontinuity nearest to the nucleus. This demonstrates that this discontinuity is indeed a strong shock which is the result of an overpressure which has built up in the entire lobe over time. Additionally, we demonstrate that if the mean free path for ions to transfer energy and momentum to the electrons behind the shock is as large as the Spitzer value, the electron and proton temperatures will not have equilibrated along the SW boundary of the radio lobe where the shock is strongest. Thus the proton temperature of the shocked gas could be considerably larger than the observed electron temperature, and the total energy of the outburst correspondingly larger as well. We investigate this using a simple one-dimensional shock model for a two-fluid (proton/electron) plasma. We find that for the thermodynamic parameters of the Cen A shock the electron temperature rises rapidly from ~ 0.29 keV (the temperature of the ambient ISM) to ~ 3.5 keV at which point heating from the protons is balanced by adiabatic losses. The proton and electron temperatures do not equilibrate in a timescale less than the age of the lobe. We note that the measured electron temperature of similar features in other nearby powerful radio galaxies in poor environments may considerably underestimate the strength and velocity of the shock.

Subject headings: galaxies: individual (Centaurus A) - X-rays: galaxies - galaxies: ISM - hydrodynamics - galaxies: jets

1. Introduction

Radio galaxies are believed to evolve through three phases. Initially, the lobes surrounding the jets are greatly overpressured relative to the ambient medium and the inflation of lobes is highly supersonic. The early, highly supersonic phase of lobe inflation is short-lived in most sources and has been conclusively identified in only a small number of radio galaxies and clusters of galaxies including Centaurus A (Kraft *et al.* 2003) and NGC 3801 (Croston, Kraft, & Hardcastle 2006). As the inflation continues and the bubbles become larger, the pressure in the lobes drops and approaches equilibrium with the ambient gas. In these systems, such as Hydra A (Nulsen *et al.* 2005) and M87 (Forman *et al.* 2005), the weak shock surrounding the lobe is often observable as a surface brightness discontinuity in the X-ray emission. Ultimately, the bubble loses energy (via adiabatic expansion and perhaps thermal conduction) as it rises buoyantly in the atmosphere and becomes effectively unobservable, although these late-stage bubbles (radio relics) may become re-energized by mergers (Reynolds *et al.* 2002; Enßlin 2002).

The proximity of Centaurus A ($d \sim 3.4$ Mpc, five times closer than the Virgo cluster,

see Israel 1998) makes it an ideal astrophysical laboratory. Features can be observed with a sensitivity and linear resolution unattainable in any other active galaxy, allowing detailed study of the hydrodynamics and energetics of lobe inflation. In our previous paper on the X-ray emission from the southwest radio lobe of Centaurus A, we reported the discovery of a hot (~ 3.5 keV) shell of X-ray emission surrounding the lobe. We interpreted this shell as the result of the highly supersonic expansion/inflation ($M \sim 8$) of the lobe into the ambient ISM. The dynamics of this process are of great interest because they can yield information on the transport physics of the ICM of clusters of galaxies and early-type galaxies, and on the roles that viscosity and thermal conduction play in the release of energy into cool cluster cores.

In this paper, we present results from an analysis of four *Chandra* pointed observations of Centaurus A, focusing on the morphology and temperature structure of the X-ray shell around the SW radio lobe. The combined observation time of the data presented in this paper is 150 ks, more than double that used in the analysis of Kraft *et al.* (2003), and the detector roll angle and pointing of the later observations are better suited to study the lobe. As a result we can study the details of the transport processes in the lobe shock on scales previously observable only in Galactic or Magellanic supernova remnants. We report two important new results. First, the surface brightness discontinuity between the SW radio lobe and the ISM extends around most of the periphery of the lobe, not just the SW corner as reported by Kraft *et al.* (2003). We find marginal evidence for a temperature gradient in the shocked gas across the X-ray bright enhancement at the southwestern boundary of the radio lobe. Second, we demonstrate that if the thermal equilibration time of the electrons and ions in the gas is as slow as the Spitzer rate, the electrons will not have thermalized. This suggests that the electron temperature inferred from the X-ray spectra considerably underestimates the strength of the shock, as has been reported for several Galactic and Magellanic SNRs. In addition, we detect sharp surface brightness discontinuities around the NE radio lobe, but lack sufficient source counts to accurately determine its gas density and temperature. The features have temperatures above 1 keV, and thus with their morphologies and locations, are suggestive of shocks.

This paper is organized as follows. Section two contains a summary of the observational details. We present the results of the data analysis in section 3, and we discuss the implications in section 4. Section 5 contains a brief summary and conclusions, as well as possible future observations. We assume a distance of 3.4 Mpc to Cen A (Israel 1998) for consistency with our previous work. At this distance, $1''=17$ pc. All uncertainties are at 90% confidence unless otherwise stated, and all coordinates are J2000. All elemental abundances in this paper are relative to the Solar abundances tabulated by Anders & Grevasse (1989).

2. Data Analysis and Methods

Centaurus A has been observed four times with *Chandra*/ACIS, twice with ACIS-I for ~ 35 ks each in AO-1, and twice with ACIS-S for ~ 50 ks each in AO-3 and AO-4 at the same roll angle. Results on the southwest lobe from the first two ACIS-I observations have been published in Kraft *et al.* (2003). The additional observations more than double the effective exposure. Results from the additional observations on the jet have already been published (Hardcastle *et al.* 2003; Kataoka *et al.* 2006). We filtered all data for periods of high background, and removed events occurring at node boundaries. The total good times of the ACIS-S and ACIS-I observations are ~ 94 ks and ~ 68 ks, respectively. The four data sets were coaligned relative to each other to better than $0.1''$ by centroiding the positions of 30 bright X-ray binaries within $5'$ of the nucleus. The absolute position was then fixed by aligning the radio and X-ray centroid of the nucleus. A comparison of the positions of X-ray binaries and globular clusters demonstrates that the absolute sky coordinates are accurate to better than $0.5''$ (Woodley *et al.* 2007, submitted). All four data sets are used for spectral analysis, but only the two ACIS-S observations are used for images and surface brightness profiles presented in this paper. The advantage in signal to noise that might be gained from combining the ACIS-S and ACIS-I observations is more than offset by the complexities of interpreting the imaging analysis of data taken at different instrument rolls. Cen A lies at relatively low Galactic latitude ($b=19^\circ.4$) and behind the North Polar Spur. The ACIS blank sky backgrounds, created from multiple observations at high galactic latitude, are inappropriate for these observations. Local background is used for all spectral analysis.

3. Results

An adaptively-smoothed, exposure-corrected, background subtracted X-ray image created from the two *Chandra*/ACIS-S observations in the 0.5-2.0 keV band, with 13 cm radio contours overlaid, is shown in Figure 1. It was not possible to remove all the detector artifacts from this image, and the dark bands running NW/SE just beyond the NE lobe and through the middle of the SW lobe are chip gaps. A raw X-ray image in the same energy band is shown in Figure 2. An X-ray enhancement surrounds most of the lobe as denoted by the white arrows in Figure 2, and is visible in both images. In our previous paper, we found that the temperature of this hot shell at the periphery of the SW lobe is ~ 3.5 keV. Since the temperature of the ISM is ~ 0.3 keV (Kraft *et al.* 2003), the inflation of the lobe is driving a strong shock into the ISM, at least toward the SW.

3.1. SW Radio Lobe

The new, deeper Chandra observations of Centaurus A show details of the structure of this high Mach number shock that were not visible in the shorter ACIS-I observations. First, it is clear from Figure 2 that the surface brightness discontinuity between the ISM and shocked gas is visible around $\sim 3/4$ of the periphery of the lobe. This suggests that the lobe is inflating more or less spherically (i.e. energy dominated), and is not simply being driven by jet ram pressure radially away from the nucleus (i.e. momentum dominated). This is consistent with the fact that the minimum pressure of the radio lobe greatly exceeds the pressure of the ISM (Kraft *et al.* 2003). The shock is strongest (in the sense that the electron temperature of the post-shock gas is highest, ~ 3.5 keV) at the southwestern edge of the lobe, where the ambient gas density is lowest.

The effect of the shock propagating in a region of denser gas can clearly be seen in the vicinity of the northern periphery of the lobe in Figures 2 and 3. Sharp discontinuities in the X-ray surface brightness are labeled S1 and S2. The sharpness of these features strongly suggests that they are due to shocks being driven into the ISM by the lobe expansion. S1 is roughly twice as bright as S2, but the ISM behind S1 is also brighter than that behind S2. Thus the X-ray surface brightness of the shocked gas is highest where the ambient density of the ISM is highest. In addition, [O III] emission lines have been detected in this region (Joss Bland-Hawthorn, private communication, 2006), suggesting that the lobe is shock-heating the multi-phase ISM of the merging spiral galaxy. The details of this will be presented in a future publication.

We extracted spectra from five regions: two rectangular regions corresponding to S1 and S2, two regions southeast of S1 and S2 (labeled PS1 and PS2), and one region in front of (i.e. in the sense of propagation of the shock, north-northwest of) S1 and S2 (labeled US1 in Table 1). The SW lobe is commonly believed to lie behind the plane of the sky containing the nucleus (Israel 1998; Tingay *et al.* 1998), so that any line of sight through regions PS1 and PS2 passes through unshocked ISM, a thin shell of shock heated gas, and the radio lobe (not visible in the X-ray band). We interpret regions PS1 and PS2 as dominated by unshocked ISM that lies along the line of sight between us and the lobe. The lobe is probably expanding spherically, and the shocked gas S1 and S2 are just breaking out of the dense gas of PS1/2 as the lobe inflates to the north. Any line of sight through regions PS1 or PS2 likely pass through two thin layers of the shock-heated shell, but the path lengths through the shell are much shorter than through the ISM, so the best fit gas temperature is representative of the ISM. The hot, shocked heated shell isn't visible over the ISM through these lines of sight. Emission from the shocked gas is much more prominent in S1 and S2, however, because our line of sight through them is nearly tangent to the shock front, maximizing its path length.

We fitted single temperature, absorbed APEC models to the spectrum of each region. Background was determined from a distant region. Visual examination of archival HST/ACS data indicates that there is absorption by cold gas in these regions, so we allowed the value of the column density to vary freely, although the minimum was fixed at the Galactic value. The elemental abundance, Z , was held fixed at the Solar value. The abundance is poorly constrained if allowed to vary freely as it can be traded off against the normalization since the emission is line dominated. We feel that fixing the abundance at the Solar value is a reasonable approximation since the lobe is likely to be expanding into gas of the merging spiral galaxy. Since the emission is line dominated, the proton density, n_p , of these features scales as $\sim Z^{-1/2}$. The results of the fits for all five regions are summarized in Table 1. The spectral fits show a clear jump in temperature at S1 and S2, compared to US1, PS1, or PS2, conclusively demonstrating that these surface brightness discontinuities are due to gas that has been heated and compressed as a result of crossing a shock front.

For spectral analysis on larger scales, we divided the southwest radio lobe into the five regions shown in Figure 4. The bright enhancement at the southwest boundary of the lobe, region 1, has been subdivided further into three regions, referred to as 1a, 1b, and 1c, for spectral analysis. Figure 5 contains a plot of the surface brightness profile of the southwest lobe in a 60° sector centered on the lobe. The regions 1a, 1b, and 1c are shown. We fit the spectrum of each region using a single temperature APEC model with Galactic ($N_H=8\times 10^{20} \text{ cm}^{-2}$) absorption and fixed the elemental abundance, Z , at 0.5 times the Solar value. Again, the elemental abundance is poorly constrained if allowed to vary freely. Unlike the interior region, however, the derived proton densities are only a weak function of the elemental abundance as the emission is continuum dominated. We chose a lower value for the abundance here as the lobe is expanding into gas of the elliptical galaxy that is unlikely to have been enriched/contaminated by the merging spiral galaxy. The best-fit temperatures and 90% uncertainties for our spectral fits are contained in Table 2. Local background was determined near the lobe. We restricted the energy band of the fit to 0.5 and 3.0 keV in order to minimize contamination from the wings of the PSF of the bright nucleus (which dominates the background above 3 keV over most of the FOV), although our results are statistically unchanged if the fit bands are extended to 5 keV.

Along the periphery of the lobe, the single temperature fits for regions 3 through 5 are poor with significant residuals seen between 0.6 and 1.0 keV, the Fe L shell complex of emission lines. We fit these data with two temperature APEC models (with Galactic absorption), and while the fits are improved, the error bars are so large that no definitive conclusions can be drawn. This suggests that the emission-line temperature may be somewhat less than the continuum electron temperature (i.e. that the electrons have not thermalized with the ions and have not reached collisional ionization equilibrium). We also fitted these data with a

non-equilibrium ionization model (‘nei’ in XSPEC 12.0) with the elemental abundances fixed at 0.5 times Solar. The fits were not greatly improved, and still formally unacceptable. We conclude that the spectra of regions 3 through 5 are not well described by single temperature thermal models, but multi-temperature and non-equilibrium ionization model provide little improvement. This suggests a temperature and ionization structure that is too complex to be resolved using the existing data.

3.2. NE Radio Lobe

We also detect sharp surface brightness discontinuities associated with the NE radio lobe. Two arcs of X-ray emission, labeled N1 and N2 in Figure 6, are located along the periphery (N1) and the interior in projection (N2) of the lobe. The morphology and location of N1 suggests a shock which would imply that the NE lobe is expanding supersonically into the ISM, similar to the SW lobe. The minimum pressure of the NE lobe greatly exceeds any plausible pressure of the ambient ISM. This conclusion is less clear for N2 as it overlies the lobe in projection. The spectra of both regions are poorly fit by single temperature APEC models, although there is considerable flux above 1 keV in both, implying gas temperatures >1 keV.

It is surprising that the radio morphologies and minimum pressures of the NE and SW lobes are so similar, but their effect on the ambient ISM is so different. Infrared synchrotron emission has been detected from the NE lobe (Brookes *et al.* 2006; Hardcastle, Kraft, & Worrall 2006), so the jet is still actively accelerating particles to relativistic velocities in this lobe. Several compact X-ray and radio knots in the SW lobe strongly suggest collimated flow in this direction as well, even if there are no structures that we can definitively term a jet (Hardcastle *et al.* 2003). The one significant difference between the lobes is that the NE lobe appears to be connected to the Northern Middle Lobe (NML) through the large-scale jet (Morganti *et al.* 1999). How in detail the inner jet, NE lobe, large scale jet, and NML are related is unclear, but it is almost certainly connected to why we don’t see a bright, strong shock around the NE lobe. In particular, the energy and momentum of both the jet and the counterjet must be comparable (otherwise the jet would push the SMBH out of the nucleus on a short timescale). However, the collimated flow from the AGN to the SW is inflating a hot bubble, whereas the flow to the NE is travelling almost losslessly (the luminosity of the X-ray jet is small compared with the mechanical power of the jet) beyond the NE lobe.

4. Interpretation

4.1. Temperature Structure

4.1.1. Northern periphery of SW lobe

The sharp surface brightness discontinuity and the temperature jump at regions S1 and S2 and in the SW demonstrate that the lobe is expanding supersonically in the plane of the sky, and hence is likely to be expanding supersonically in all directions. The velocity of the shocks between S1/S2 and the undisturbed ISM can be estimated from the ratio of the pre-shock to post-shock temperatures. It is not clear if regions PS1/PS2 or US1 should be used to determine the thermodynamic parameters of the unshocked gas. The complex morphology of the X-ray surface brightness, combined with spatial variability in the unshocked gas temperature and absorption and uncertainties in the three dimensional distribution of the gas make determination of the density profile virtually impossible. However, the gas temperatures of PS1, PS2, and US1 are identical, so we can make some quantitative statements about the energetics and dynamics of the shocks without full knowledge of the density profile.

The ratio of post-shock to pre-shock gas temperatures, T_R , as a function of Mach number is (for a purely hydrodynamic shock and $\gamma=5/3$)

$$T_R = T_2/T_1 = (5M_1^2 - 1)(M_1^2 + 3)/(16M_1^2), \quad (1)$$

where T_2 and T_1 are the post and pre-shock gas temperatures, respectively, and M_1 is the Mach number of the flow in the pre-shocked gas. These temperature ratios are 2.7 ± 0.5 and 2.8 ± 0.7 for regions S1 and S2, respectively, at 90% confidence assuming the pre-shock gas temperatures of PS1 and PS2, respectively. The Mach numbers are then 2.4 ± 0.3 and 2.5 ± 0.5 . The uncertainties on the Mach numbers are large because the fractional uncertainties on the pre-shock gas temperature are large. The velocities of the shocks S1/S2 and the undisturbed ISM are $\sim 600\pm 75$ and 680 ± 140 km s⁻¹, respectively. Assuming that the pressure of the lobe is uniform (a good assumption as the sound speed of the lobe plasma is likely orders of magnitude larger than the thermal gas), the ratio of the pre-shock density of S1 to that of S2 is 1.3 ± 0.3 based on their relative surface brightnesses. We point out that the lower shock temperature of PS1 and PS2 relative to the regions more distant from the nucleus (1 through 5) is also qualitatively consistent with a picture where the nearly isobaric lobe is expanding more slowly into the denser regions of gas near the nucleus.

4.1.2. SW periphery of SW lobe

As discussed in Kraft *et al.* (2003), we model the emission as a shell of uniform density rotated to our line of sight. In Figure 5, we have labeled the approximate positions of the contact discontinuity between the shocked gas and radio lobe (the red dashed line on the left), the shock-heated shell (the region between the two dashed red lines), and the transition region (the actual thickness of the shock, see below for detailed discussion - labeled 1a). We estimate the thickness of the shell and the transition region to be $\sim 28''$ (476 pc) and $\sim 9''$ (153 pc), respectively. The distance from the shock to the contact discontinuity is therefore $\sim 37''$ (630 pc). The width of the transition region is estimated as the distance over which the surface brightness of the shell goes from the background level to its peak value. This is an upper limit on the actual thickness of the transition region as we have neglected projection effects. The ratio of the gas temperature in region 1b to region 1c is 0.72 ± 0.20 (90% confidence). Thus the temperature of the gas closest to the shock is cooler (at marginal significance) than the gas behind the shock closer to the lobe. We have neglected the effects of projection, but projection would tend to wash out any temperature differences, so our estimate of the temperature ratio is really an upper limit. The temperature of the material in the transition region (region 1a) is poorly constrained, but is > 2.5 keV at 90% confidence. Thus the transition region is not significantly cooler than regions 1b or 1c. A detailed map of the temperature structure of this shock-heated shell would permit us to make a strong statement about the limits of the applicability of a purely hydrodynamical model to the lobe/ISM interaction as we argue below.

4.2. Transport Processes and Electron-Ion Equilibration in the Shock around the SW Radio Lobe

4.2.1. Theoretical Considerations

It is almost always assumed that the physics governing radio lobe/ICM interactions is purely hydrodynamic. That is, the electron-ion plasma can be considered as a single, classical fluid. This may not be a good approximation for the high Mach number shock around the SW radio lobe of Cen A because of its proximity, temperature, and density. The mean free path, λ_{ii} , for collisional energy exchange between the ions (protons) is

$$\lambda_{ii} = 230 pc \times (T_i/10^7 K)^2 (n_p/10^{-3} cm^{-3})^{-1}, \quad (2)$$

where T_i and n_p are the ion temperature and density, respectively (Spitzer 1962). For simplicity we assume that the plasma is pure hydrogen. The great bulk of the gas kinetic

energy is carried into the shock by the ions. In a strong, collision-dominated shock the kinetic energy is thermalized among the ions over a distance comparable to λ_{ii} . Collisional energy exchange between the ions and electrons is a factor of $\sim \sqrt{m_p/m_e} \simeq 43$ slower, so that the region over which the electron temperature differs significantly from the ion temperature is roughly 40 times larger than the thickness of the ion shock. At the observed temperature of $\sim 3.5\text{--}4.0$ keV, the ion shock around the SW radio lobe of Cen A should be spatially resolvable. A plot of the predicted thickness of the transition region as a function of post-shock temperature is shown in Figure 7 for the measured gas density ($n_p = 2.2 \times 10^{-2} \text{ cm}^{-3}$) of the shell. The temperature of the gas in the southwest region of the shell (Region 1 of Table 2) is 3.9 ± 0.7 keV (for $Z=0.5$, 90% confidence). The region of allowed parameter space for ion-ion (solid) and ion-electron collisions (dashed) is denoted by the vertical dashed lines in Figure 7. Thus the thickness of the ion shock around the lobe would be several arcseconds at the distance of Cen A. The distance scale for ion-electron equilibration is also shown in Figure 7. Around the SW lobe in Cen A, this would be more than 1 kpc, which is larger than the thickness of the shell.

Observations of young Galactic and Magellanic supernova remnants (SNRs) demonstrate that the ion shocks are collisionless (Rakowski 2005), therefore the ion shock in Cen A is likely to be orders of magnitude smaller than estimated from ion-ion collisions. Plasma effects and magnetic fields, even if not dynamically important, can reduce the mean free path for energy and momentum transfer between *ions* to a value many orders of magnitude smaller than the Spitzer estimate. The ion shock of Galactic supernova remnants (~ 1000 times closer than Cen A) with gas temperatures similar to the shock-heated shell in Cen A have never been spatially resolved. It would therefore be surprising if we could observe this region in Cen A.

However, the efficiency with which the protons transfer energy to the electrons in SNR shocks (and in low density, high Mach number plasma shocks in general) is largely unknown. There may be some collisionless heating of the electrons in the ion shock, but it is believed that this heating will not be efficient and that the electron temperature will be significantly below the ion temperature at the boundary of the ion shock (i.e. where the protons reach their final, post-shock temperature) (Bagenal, *et al.* 1987; Cargill & Papadopoulos 1988; Schwartz, *et al.* 1988). The plasma (i.e. wave-particle interaction) and MHD processes that reduce λ_{ii} in the ion shock of SNR shocks do not appear to greatly reduce λ_{ie} . In fact, large differences between the electron and ion temperatures have been measured in several young SNRs including SN 1006 (Vink *et al.* 2003), Tycho, the Cygnus Loop (Raymond *et al.* 2003), and the LMC remnant Dem L71 (Rakowski, Ghavamian, & Hughes 2003). Comparison of X-ray measurements of electron temperatures, T_e , with H_α/H_β line ratio estimates of the ion temperature, T_i , indicates that there is a strong correlation between the shock

velocity and the ratio of T_e to T_i (Rakowski 2005). Stronger shocks in young SNRs tend to have lower ratios of T_e/T_i . For Cen A, the ratio of the temperature of the gas in the shell (~ 3.5 keV) to the ISM (0.3 keV) is ~ 12 . This temperature ratio implies a shock velocity (for a purely hydrodynamical shock) of ~ 1500 km s $^{-1}$ ($M \sim 6.2$). For SNR with a similar shock velocity such as Tycho, $T_e/T_i \sim 0.2$. Therefore, if the transport processes relevant to the expansion of the SW radio lobe of Cen A are similar to those in young SNRs, it is likely that the proton temperature is considerably higher than the electron temperature, and the electron temperature (i.e. the temperature that we measure with the X-ray spectrum) considerably underestimates the strength of the shock.

Therefore, the electrons and ions are unlikely to have reached thermal equilibrium and there should be an observable radial temperature gradient in the shell. Additionally, since we measure the electron (and ionization) temperature with the X-ray spectrum, it is likely that we have underestimated the ion temperature and shock velocity, so the shock may be even stronger than we estimate based on the electron temperature. A time-dependent consideration of Coulomb collisions in plasmas suggests that the ratio, q , of the electron temperature, T_e , to the final (equilibration) temperature T_f , after time t is given by

$$dq/dt = Kq^{-3/2}(1 - q), \quad (3)$$

where $K = 2.75 \times 10^{-4} n (T_f / 10^7 K)^{-3/2}$ yrs $^{-1}$ and n is the total (i.e. $n_e + n_i$) particle density (Spitzer 1962). Thus the electron temperature would rise to roughly half the ion temperature in a few times the Spitzer ion-ion collision length (tens of arcseconds in our case), then more slowly approach equilibrium over a distance $43 \times \lambda_{ii}$

4.2.2. Simulations

To evaluate this phenomenon quantitatively, we created a one dimensional spherical shock model in a two fluid (electron/proton) plasma driven by energy injected from the center. Several simplifying assumptions have been made. First, we assume energy is transferred between the particles only by Coulomb collisions, and that the rate of energy transfer is given by the Spitzer value. Second, we assume that there is no separation between the electrons and ions (i.e. $n_e = n_i$). This latter approximation is extremely good as the maximum length scale of separation is on the order of the Debye length, which is hundreds of meters for the parameters of the Cen A shock. Third, we introduce an artificial proton viscosity (the Richtmyer-Morton artificial viscosity) to ensure that we capture the features of the shock at the resolution of the simulation. Finally, we neglect the effects of thermal conduction. More detailed studies of two-fluid shocks demonstrate that thermal conduction from

the downstream electrons can heat the pre-shock electrons, thus creating a shock precursor (Casanova *et al.* 1991). The presence of such a precursor has not been seen in Galactic SNRs, and is unobservable in our data. We emphasize that we are interested in studying the thermal relaxation between the ions and electrons, not thermal conduction.

Under these conditions, motion of the two fluids is described by a single continuity equation

$$\frac{d\rho}{dt} + \rho \nabla \cdot \mathbf{v} = 0, \quad (4)$$

where ρ is the total density and \mathbf{v} is the common velocity of the two fluids. The lagrangian time derivative has its usual meaning, $d/dt = \partial/\partial t + \mathbf{v} \cdot \nabla$. The single momentum equation is

$$\rho \frac{d\mathbf{v}}{dt} = -\nabla p + \nabla \cdot \mathbf{T} + \rho \mathbf{g}, \quad (5)$$

where p is the total gas pressure, \mathbf{T} is the viscous stress tensor, and \mathbf{g} is the acceleration due to gravity. Only the artificial viscosity contributes to the viscous stresses in the simulation. The energy equation for the protons is

$$\rho_p \frac{d\epsilon_p}{dt} = \frac{p_p}{\rho_p} \frac{d\rho_p}{dt} + \Pi_{\text{visc}} + \xi_{pe} \quad (6)$$

and that of the electrons is

$$\rho_e \frac{d\epsilon_e}{dt} = \frac{p_e}{\rho_e} \frac{d\rho_e}{dt} + \xi_{ep}. \quad (7)$$

Here ρ_α is the density of a fluid component ($\alpha = p$ or e), p_α is the corresponding component of the pressure and ϵ_α is the specific thermal energy ($\epsilon_\alpha = \gamma p_\alpha / [(\gamma - 1)\rho_\alpha]$). By our assumptions, the viscous heating rate, Π_{visc} , only affects the protons directly. The rate of energy transfer between the fluids is

$$\xi_{\alpha\alpha'} = -nk_B(T_\alpha - T_{\alpha'})/\tau, \quad (8)$$

where the equilibration time τ is

$$\tau = \frac{3m_e m_i c^3}{8\sqrt{(2\pi)}e^4 n_e \ln\Lambda} \sim 9300 \text{ yrs} \times \frac{T_e^{3/2}(\text{keV})}{n_e(\text{cm}^{-3})}. \quad (9)$$

The factor $\ln(\Lambda)$ in the denominator of equation 9 is the Coulomb logarithm and has a weak (logarithmic) dependence on the temperature. The relative thermal speed, c , of the particles ($(\frac{k_B T_p}{m_p} + \frac{k_B T_e}{m_e})^{1/2}$) is dominated by the electrons at the electron and ion temperatures of interest in this paper. Finally, we assume an ideal gas equation of state for both the electrons and protons with $\gamma = \frac{5}{3}$.

We simulate the shock as a continuous release of energy at the center of an isothermal atmosphere with a power law density distribution. The parameters of the ambient gas were

matched to measurements of Cen A ($\beta=0.40$, $k_B T=0.29$ keV, see Kraft *et al.* (2003) for details). In our earlier paper, we found that the density jump at the shock was roughly a factor of 10, much larger than the factor of 4 required by the Rankine-Hugoniot relations for a strong shock in a fluid with $\gamma=5/3$. This large density jump cannot be accounted for in our simulations, and would require the inclusion of additional physics (e.g. the creation of cosmic rays at the shock). Conservatively, we set the ambient ISM to a higher density so that the post-shock value matches the measured density of the shell. If the density of the ISM and shell is, in fact, lower, our conclusions are strengthened as the timescales for equilibrium are even longer than in the simulations presented in this paper. Three values of the initial input energy were chosen. In the first simulation, the energy was chosen such that the Mach number ($M=8.3$) of the flow at the distance of the SW boundary of the lobe from the nucleus (~ 6.5 kpc) matches the value quoted by Kraft *et al.* (2003). Two other values were chosen, $M=5.2$ and 10.8 , to bracket this choice of Mach number. The electron temperature as a function of distance behind the shock for each of the three cases is shown in Figure 8.

In all these simulations, the proton temperature rises rapidly to roughly twice its final value, since all of the kinetic energy of the shock is initially transferred to the protons. The electron temperature then begins to rise rapidly, but levels off at about 3.5 keV (in the Mach 8.3 case), roughly 40% of the proton temperature. As the electron and proton temperatures approach each other, the rate of energy transfer decreases, ultimately being balanced by adiabatic losses as the plasma expands after passage of the shock. Thus the electron temperature reaches a plateau with very little gradient from the shock to the contact discontinuity. There is, however, a significant gradient in the proton temperature between the shock and the contact discontinuity. For the spherical model used here, all gas initially outside the cavity remains in place as the cavity expands. In a more realistic model, the shocked gas may flow around the radio lobe as the lobe pushes outward if the expansion of the lobe is largely radial from the nucleus. As a result, the shocked gas closest to the cavity would have flowed away and the remaining shell of shocked gas would be thinner than for the model. This is probably not significant for the Cen A lobe as it appears to be overpressured, and hence expanding supersonically, around the entire periphery.

4.2.3. Implications

Consideration of the transport processes thus has several important implications in the case of Cen A. First, it suggests that the proton temperature is considerably higher than the electron temperature at the strongest part of the shock. Thus our earlier estimates of the

total power of the lobe expansion may be low by a factor of up to a few. Second, the observed electron temperature is not a sensitive diagnostic of the shock velocity or the energy in the shock. In the three cases shown in Figure 8, the post shock electron temperature varies by only a factor of ~ 2 , while the initial post-shock proton temperature varies by more than a factor of 4.

Third, our simulations predict that there will be little temperature structure in the shell between the shock and the contact discontinuity except for a small region of lower temperature just behind the shock. Purely hydrodynamic simulations of a high Mach number shock around a solid sphere in a uniform density atmosphere show a $\sim 10\%$ increase in the gas temperature from the shock to the contact discontinuity. This can be easily demonstrated from Bernoulli’s equation, the non-zero velocity of the gas just behind the shock must be converted to thermal energy of the gas at the contact discontinuity. The Sedov solution for a point release of energy in an atmosphere with a power law density gradient predicts an even larger gradient. Kaiser & Alexander (1999) describe this process for a range of model atmospheres. Data of sufficient quality should be able to clearly distinguish between these alternatives.

Fourth, there will be less temperature structure around the periphery of the lobe than one would naively expect based on the Rankine-Hugoniot shock conditions. In particular, the shock will be weaker around the sides (i.e. closer to the nucleus) of the lobe since the nearly isobaric lobe is expanding into denser material. Since the shock will be weaker, and the ambient density higher, the electron and proton temperatures will equilibrate more rapidly than at the SW periphery of the lobe. The observed electron temperature of the shell nearest the nucleus will be close to the final temperature and a much better, though imperfect, diagnostic of the strength of the shock. The post-shock electron temperature (normalized to the value at the SW edge) as a function of normalized distance between the nucleus and the SW edge is shown in Figure 9. The solid curve is the normalized temperature if the shock is purely hydrodynamic, the dashed curve is for our two-fluid shock model. There is a clear difference in the temperature profiles. The point with the error bars is the measured ratio of the temperature in region 5 to that in region 1. The existing data are not adequate to distinguish between the two models at 90% confidence.

This also has important implications for similar features in other radio galaxies and clusters of galaxies. Differences in the electron and proton temperatures will make it very difficult to detect strong shocks in young, powerful radio sources. In the earliest stage of the development of a radio galaxy (i.e. when the jet is momentum dominated), the shock temperature could be tens or even hundreds of keV and the equilibration time would be tens or hundreds of millions of years. This is orders of magnitude longer than the lifetime

of the source in this stage. The proton temperature could be quite high with little or no change in the electron temperature. Finally, the importance of transport processes could have important implications for the long term evolution of powerful radio galaxies in poor environments. In these cases, the advance speed of the jet head can remain supersonic for tens or hundreds of kpc. The timescale for electron/proton equilibration could be hundreds of millions of years (or more). In the absence of other processes to transfer energy from the protons to electrons, the atmospheres of poor systems could remain far from equilibrium for a considerable period of time.

5. Conclusions

The hot thermal shell of shock-heated gas surrounding the southwest radio lobe of Centaurus A is the best example of a spatially resolvable high Mach number shock in an extragalactic system. It is therefore a unique laboratory in which to study the hydrodynamics and plasma physics of the radio lobe/ISM interaction. We find that the surface brightness discontinuity extends around $\sim 75\%$ of the boundary of the SW radio lobe. The shock likely extends around the entire lobe, but the current observations do not yet have the sensitivity to detect it. We also report the discovery of two filaments of X-ray emission associated with the NE lobe, although the data quality is not sufficient to conclusively determine if they are shock-heated gas.

We demonstrate that if the energy transfer between electrons and protons behind the shock of the SW lobe is purely collisional, their temperatures will not have equilibrated. One dimensional, two-fluid field-free simulations show there will be little temperature structure in the gas between the shock and the contact discontinuity as adiabatic losses will roughly balance Coulomb heating of the electrons. These simulations also predict significant differences in the temperature structure as a function of distance from the nucleus (i.e. around the periphery of the lobe) compared with a purely hydrodynamic model. That is, the shock strength will vary quite strongly around the lobe because of the density gradient in the gas. Our two-fluid simulations suggest that the electron temperature in the shocked gas around the lobe will be more uniform than predicted in single fluid hydrodynamic model.

A deep (>500 ks) *Chandra* observation of Cen A is required to further elucidate the underlying shock physics. In particular, a deeper observation would permit an accurate measurement of the shock temperature and pressure around the periphery of the lobe, thus constraining both the expansion velocity, external gas pressure, and external density. A deeper observation of the X-ray bright enhancement at the southwest boundary of the lobe would allow a detailed estimate of the temperature structure in the shock. This could then

be compared with two and three dimensional two-fluid simulations of the shock to better estimate the energy in the shock and the degree of coupling between the electrons and ions.

We thank John Raymond, Cara Rakowski, and Joss Bland-Hawthorn for helpful discussions. This work was supported by NASA grant NAS8-01130 (the HRC GTO grant). We also thank the anonymous referee for comments that improved this paper.

REFERENCES

- Anders E. & Grevasse N. 1989, *Geochimica et Cosmochimica Acta*, **53**, 197.
- Bagenal, R., *et al.* 1987, *J. Geophys. Res.*, **92**, 8603.
- Borkowski, K., Sarazin, C. L., & Blondin, J. M. 1994, *ApJ*, 429, 710.
- Brookes, M. H., *et al.* (2006), *ApJ*, **646**, 41.
- Cargill, P. J., & Papadopoulos, K. 1988, *ApJ*, **329**, L29.
- Casanova, M., *et al.* 1991, *Ph.Rev.L.*, **67**, 2143.
- Croston, J. A., Kraft, R. P., and Hardcastle, M. J. 2006, *ApJ*, submitted.
- Dickey, J. M., & Lockman, F. J. 1990, *ARA&A*, **28**, 215.
- Enßlin, T. 2002, *astro-ph/0206310*.
- Fabian, A. C., Sanders, J. S., Taylor, G. B., Allen, S. W., Crawford, C. S., Johnstone, R. M., & Iwasawa, K. 2006, *MNRAS*, **366**, 417.
- Finoguenov, A. & Jones, C. 2001, *ApJ*, **547**, L107.
- Forman, W. R. *et al.* 2005, *ApJ*, **635**, 894.
- Hardcastle, M. J. *et al.* 2003, *ApJ*, **593**, 169.
- Hardcastle, M. J., Kraft, R. P., & Worrall, D. M. 2006, *MNRAS*, **368**, L15.
- Israel, F. P. 1998, *Astron. Astrophys. Rev.*, **8**, 237.
- Jones, C. *et al.* 2002, *ApJ*, **567**, L115.
- Kaiser, C. R. & Alexander, P. 1999, *MNRAS*, **305**, 707.
- Kataoka, J., Stawarz, Lukasz, Aharonian, F., Takahara, F., Ostrowski, M., & Edwards, P. G. 2006, *ApJ*, **641**, 148.
- Kraft, R. P., Vázquez, S. E., Forman, W. R., Jones, C., Murray, S. S., Hardcastle, M. J., Worrall, D. M., Churazov, E. 2003, *ApJ*, **592**, 129.
- Kraft, R. P., *et al.* 2006, *ApJ*, **639**, 753.

- Landau, L. D., & Lifshitz, E. M. 1989, 'Fluid Mechanics', 2nd ed., Butterworth and Heinemann.
- Morganti, R., Killeen, N. E. B., Ekers, R. D., Oosterloo, T. A. 1999, MNRAS, **307**, 750.
- Nulsen, P. E. J., McNamara, B. R., Wise, M. W., & David, L. P. 2005, ApJ, **628**, 629.
- Rakowski, K., Ghavamian, P., & Hughes, J. 2003, ApJ, **590**, 846.
- Rakowski, C. 2005, Adv. Sp. Res., **35**, 1017.
- Raymond, J. C., Ghavamian, P., Sankrit, R., Blair, W. P., & Curiel, S. 2003, ApJ, **584**, 770.
- Reynolds, C. S., Heinz, S., & Begelman, M. C. 2002, MNRAS, **332**, 271.
- Sanders, J. S. & Fabian, A. C. 2006, MNRAS, **375**, L65.
- Schiminovich, D., van Gorkom, J. H., van der Hulst, J. M., & Kasow, S. 1994, ApJ, **423**, L101.
- Schwartz, S. J., *et al.* 1988, J. Geophy. Res., **93**, 12923.
- Spitzer, L. 1962, "Physics of Fully Ionized Gases", John Wiley and Sons, New York.
- Tingay, S. J. *et al.* 1998, AJ, **115**, 960.
- Vink, J., Laming, J. M., Gu, M. F., Rasmussen, A., & Kaastra, J. S. 2003, ApJ, **587**, L31.

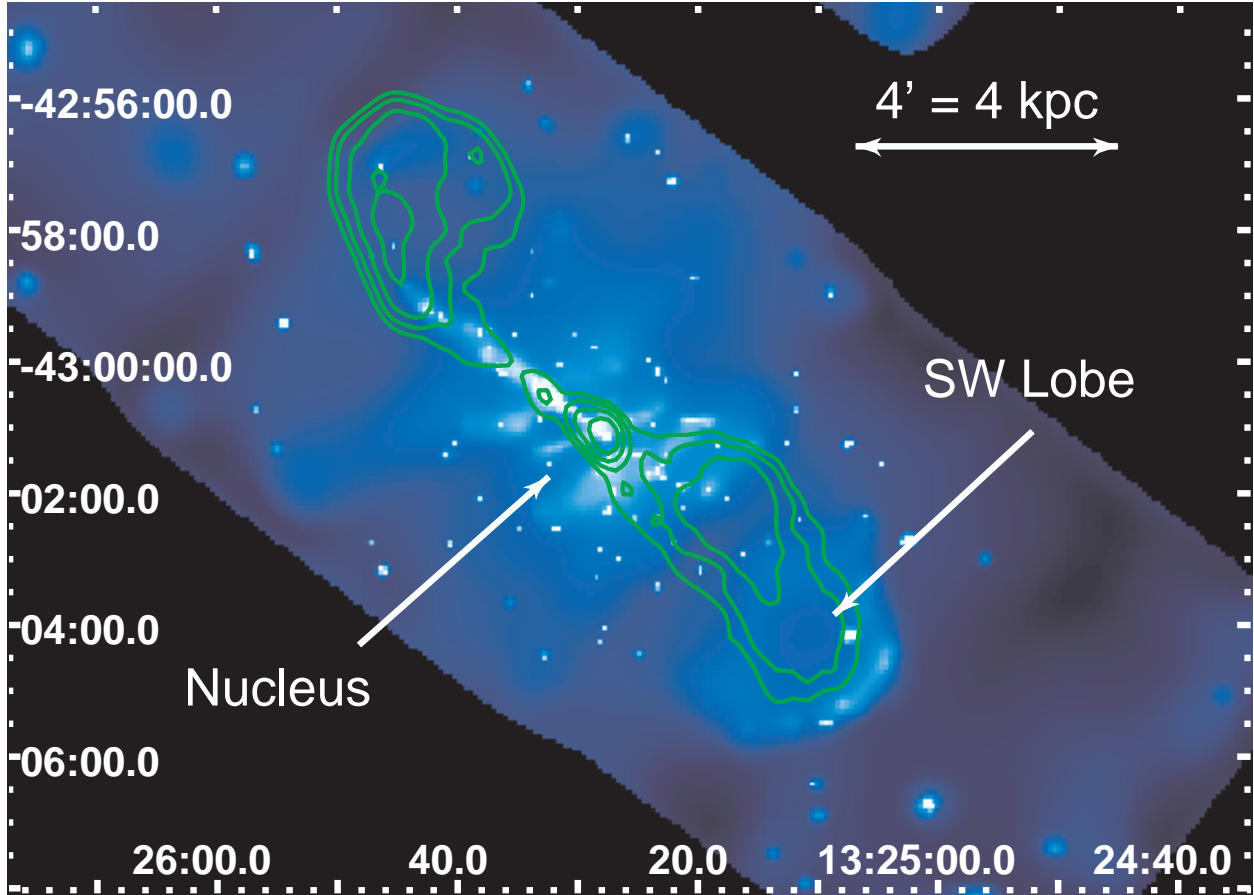


Fig. 1.— Adaptively smoothed, exposure corrected, background subtracted Chandra/ACIS-S image of Centaurus A in the 0.5-2.0 keV band. Radio contours (13 cm - $30'' \times 20''$ beam FWHM) are overlaid.

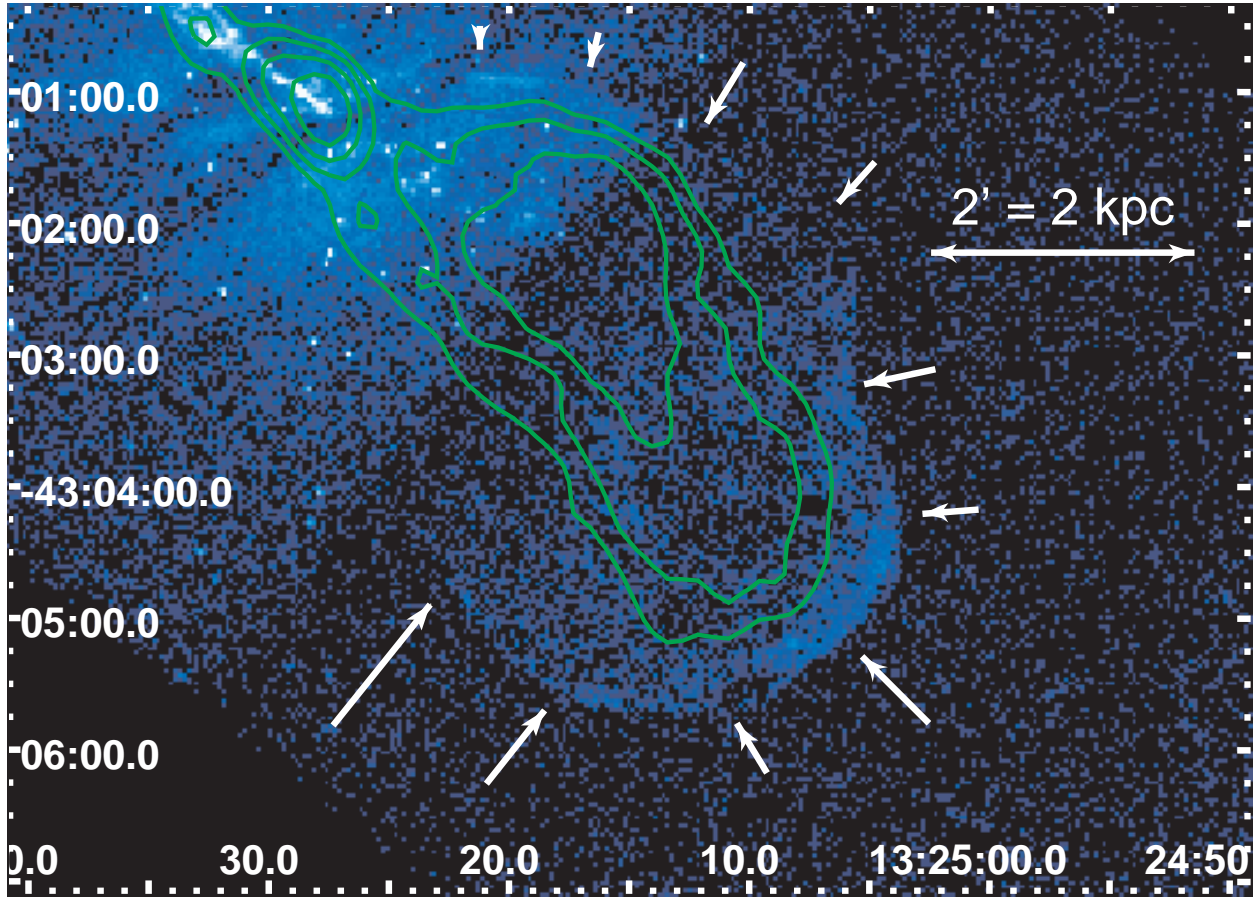


Fig. 2.— Raw X-ray image of the southwest radio lobe of Centaurus A in the 0.5-2.0 keV band. Radio contours (13 cm - $30'' \times 20''$ beam) are overlaid. The white arrows denote the surface brightness discontinuity which delineates the outer edge of the shock-heated shell of gas.

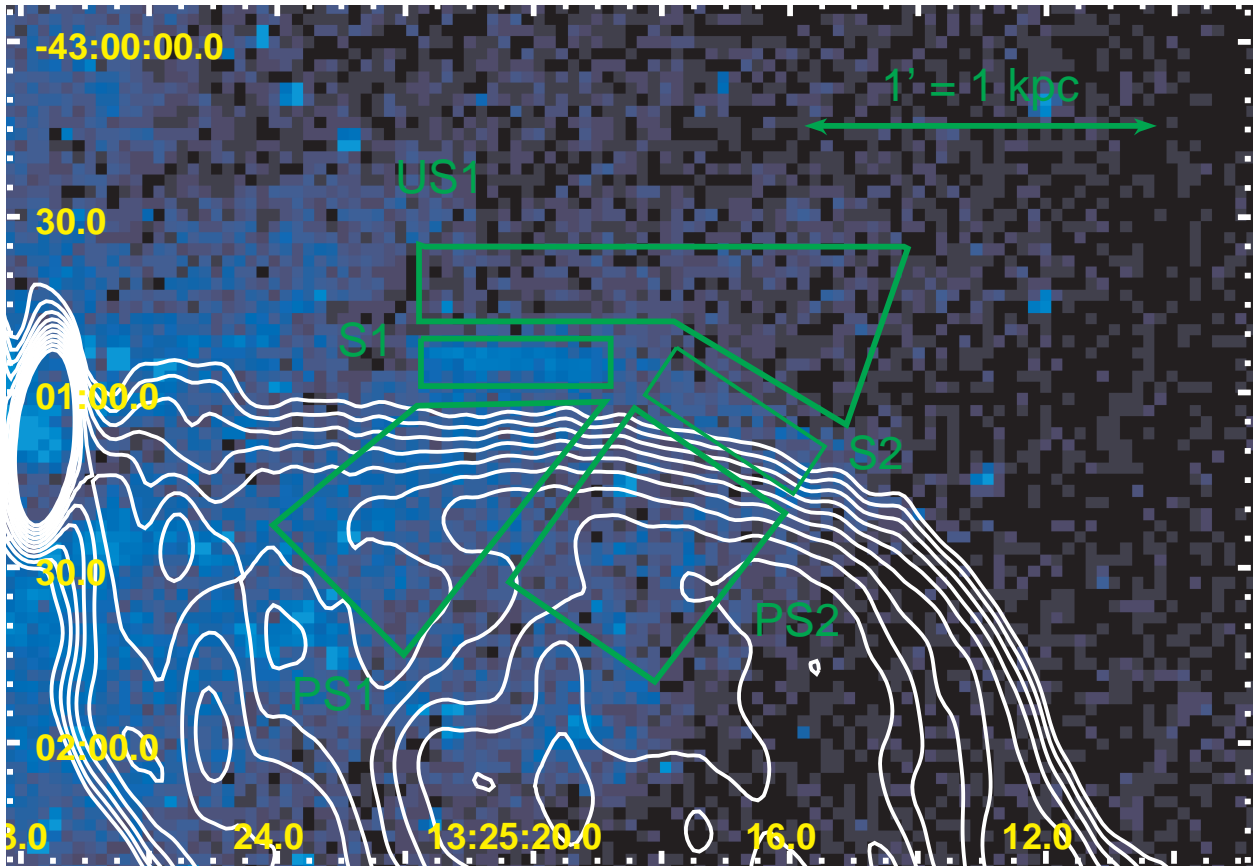


Fig. 3.— Raw X-ray image of the southwest radio lobe of Centaurus A in the 0.5-2.0 keV band showing the shock (regions S1 and S2) along the northern periphery of the lobe. Radio contours (1.54 GHz - 16.25"×4.80" beam) are overlaid.

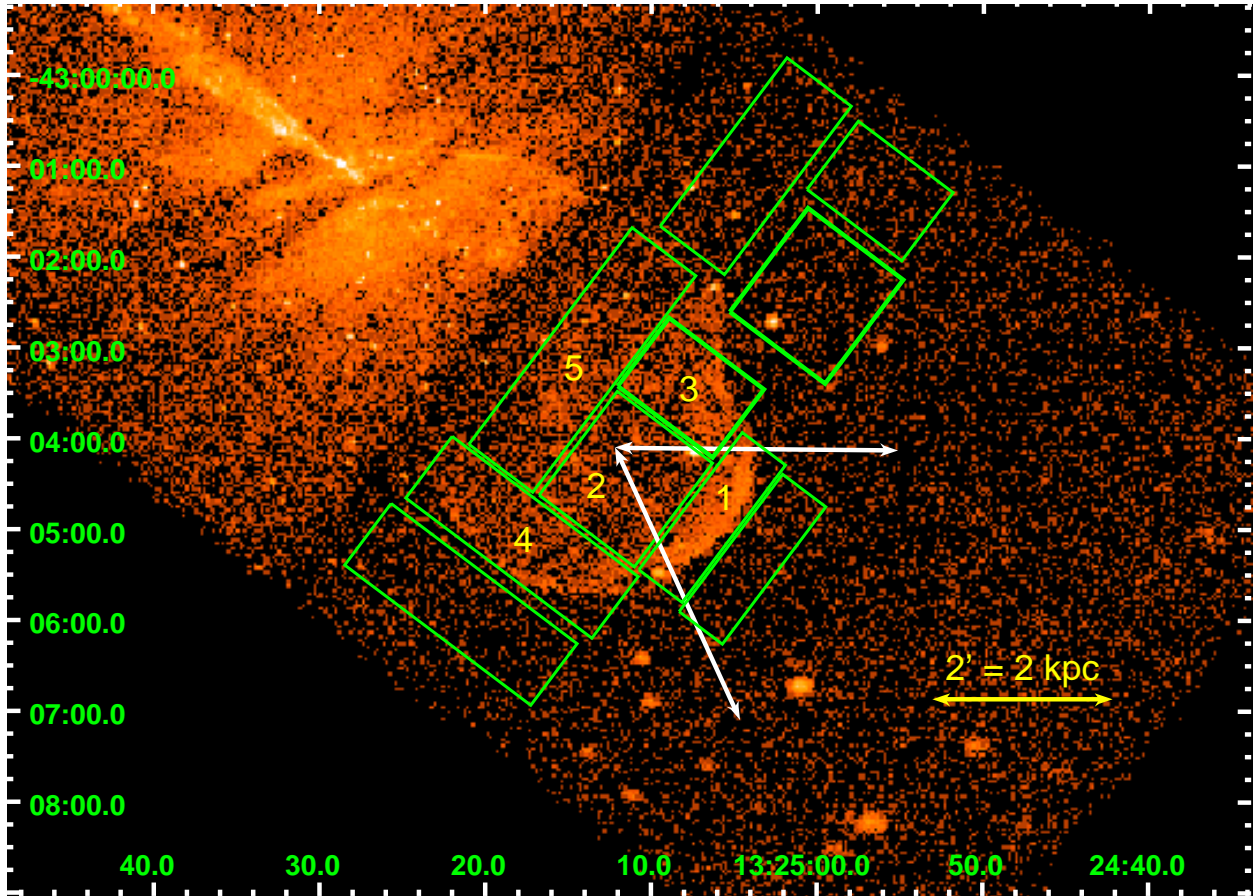


Fig. 4.— Raw X-ray image of the southwest radio lobe of Centaurus A in the 0.5-2.0 keV band showing regions used for spectral fitting and background subtraction. Region 1 was also divided into three radial subregions (1a, 1b, and 1c) as discussed in the text. The best-fit values of the fitted parameters and uncertainties are contained in Table 2. The white lines denote the approximate position of the surface brightness wedge shown in Figure 5.

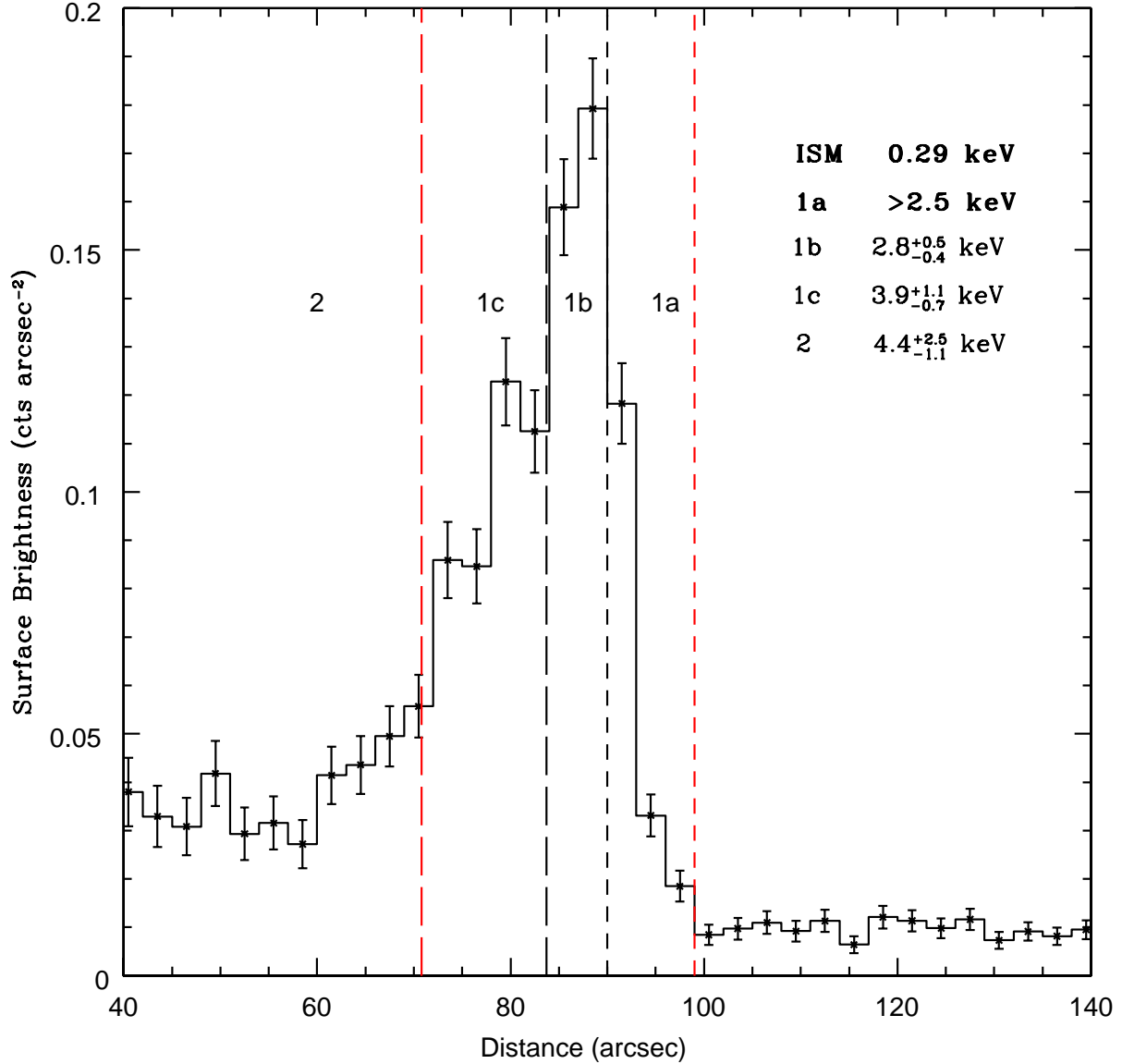


Fig. 5.— Surface brightness profile from the center of the southwest lobe in a 60° sector toward the X-ray enhancement along the southwest boundary in the 0.5-2.0 keV band. The region between the two red dashed lines is the approximate thickness of the shock (i.e. the distance between the shock and contact discontinuity defined by the edge of the radio lobe - $\sim 28''$). The regions 1a, 1b, and 1c used for spectral analysis are also identified. Error bars on the data points are 1σ uncertainties due to counting statistics. The best fit temperatures and 90% uncertainties for each of the regions is summarized on the right (see Table 2

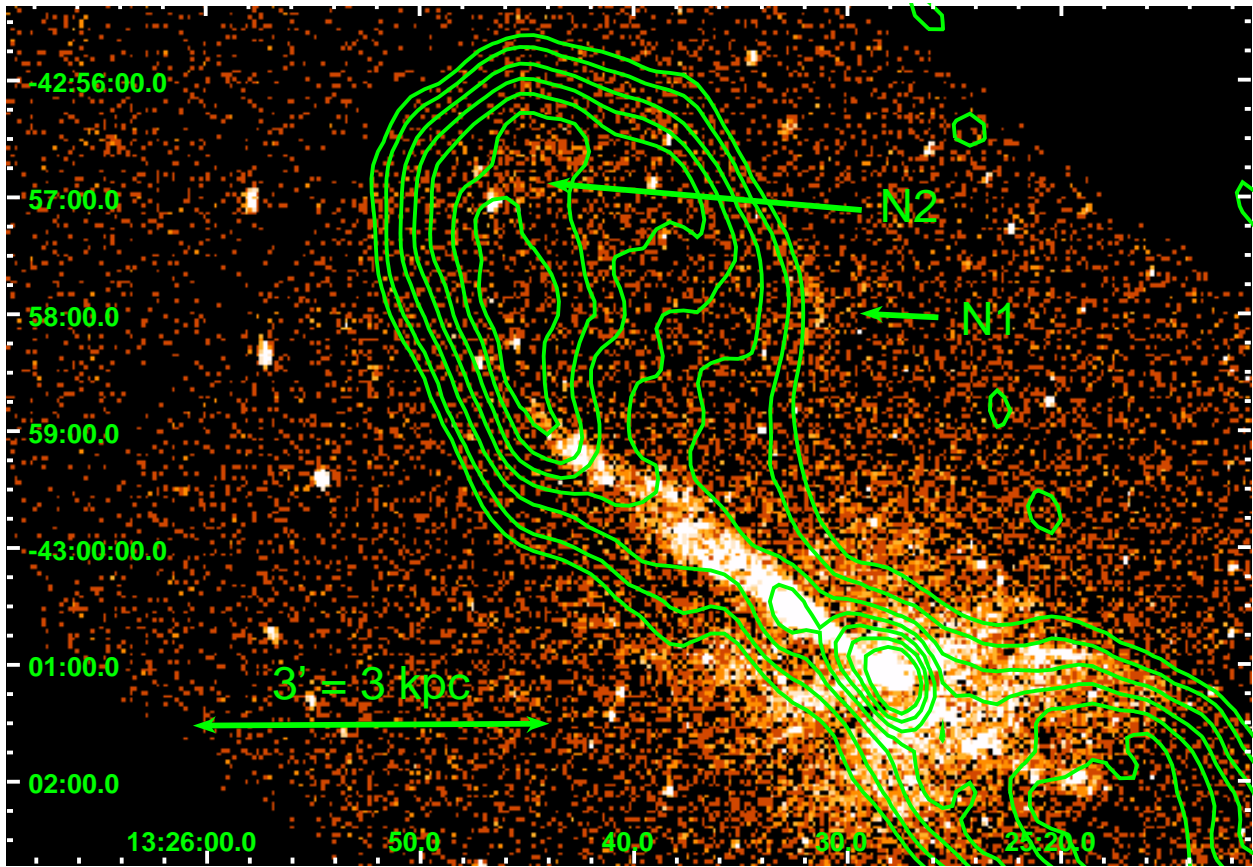


Fig. 6.— Raw X-ray image (ACIS-S, 0.5-2.0 keV bandpass) of Centaurus A with 13 cm radio contours (beam $30.4'' \times 20.3''$ FWHM) overlaid. Two X-ray enhancements described in the text are labeled N1 and N2.

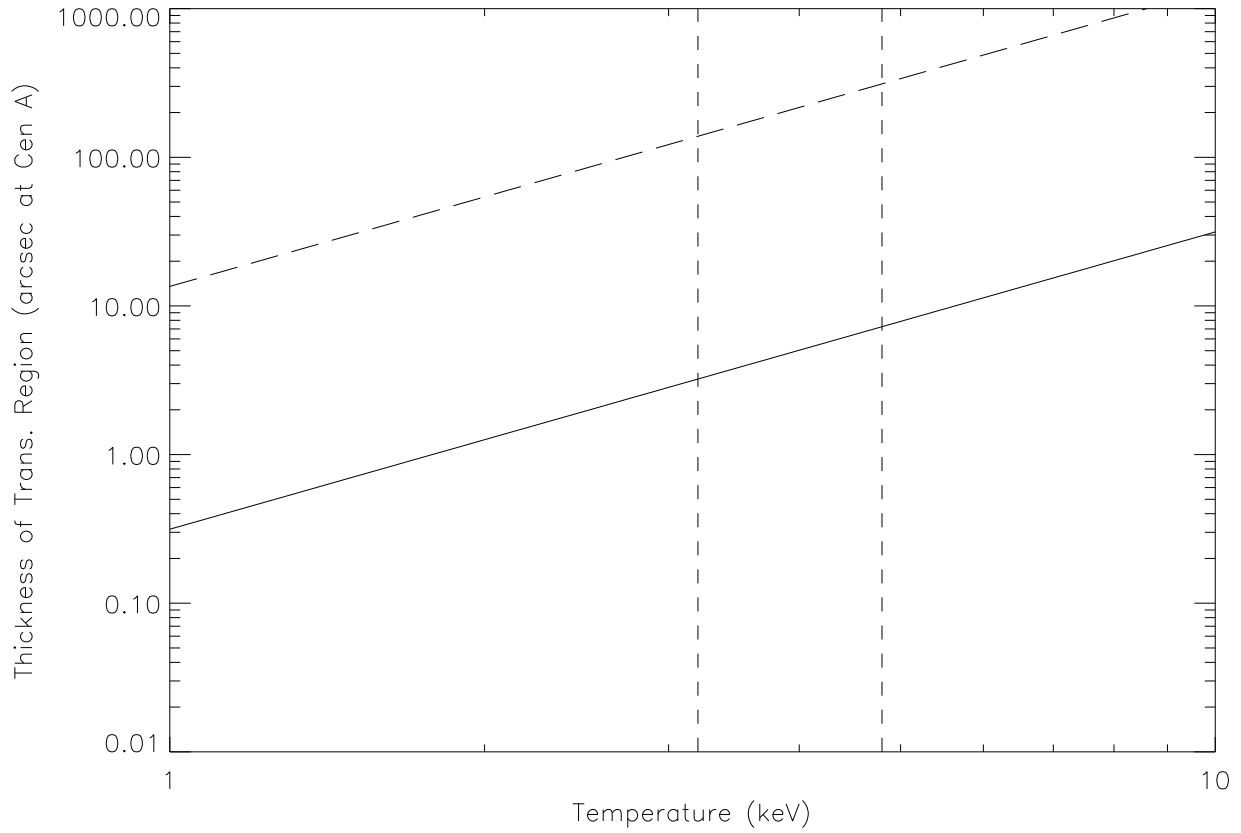


Fig. 7.— Plot of thickness of ion shock for ion-ion collisions (solid curve) and ion-electron collision equilibration length (dashed curve) for shock around the southwest radio lobe of Centaurus A assuming the energy transfer between particles is governed by Coulomb collisions at the Spitzer rates. The vertical lines denote the upper and lower limits (90% confidence) of the temperature of the shell.

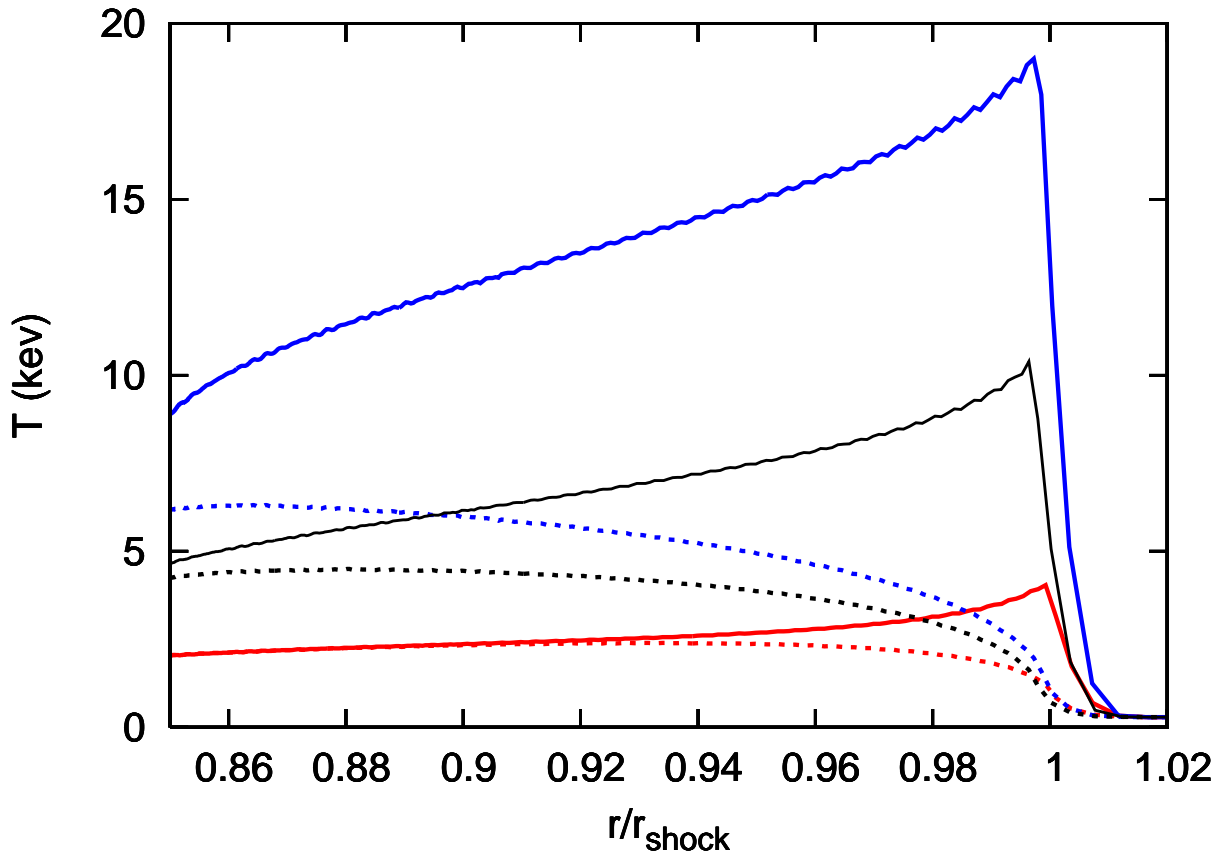


Fig. 8.— The proton (solid lines) and electron (dashed lines) temperatures as a function of distance behind the shock of the two fluid shock model for three Mach numbers. The blue, black, and red curves correspond to shock Mach numbers of 10.8, 8.3, and 5.2, respectively.

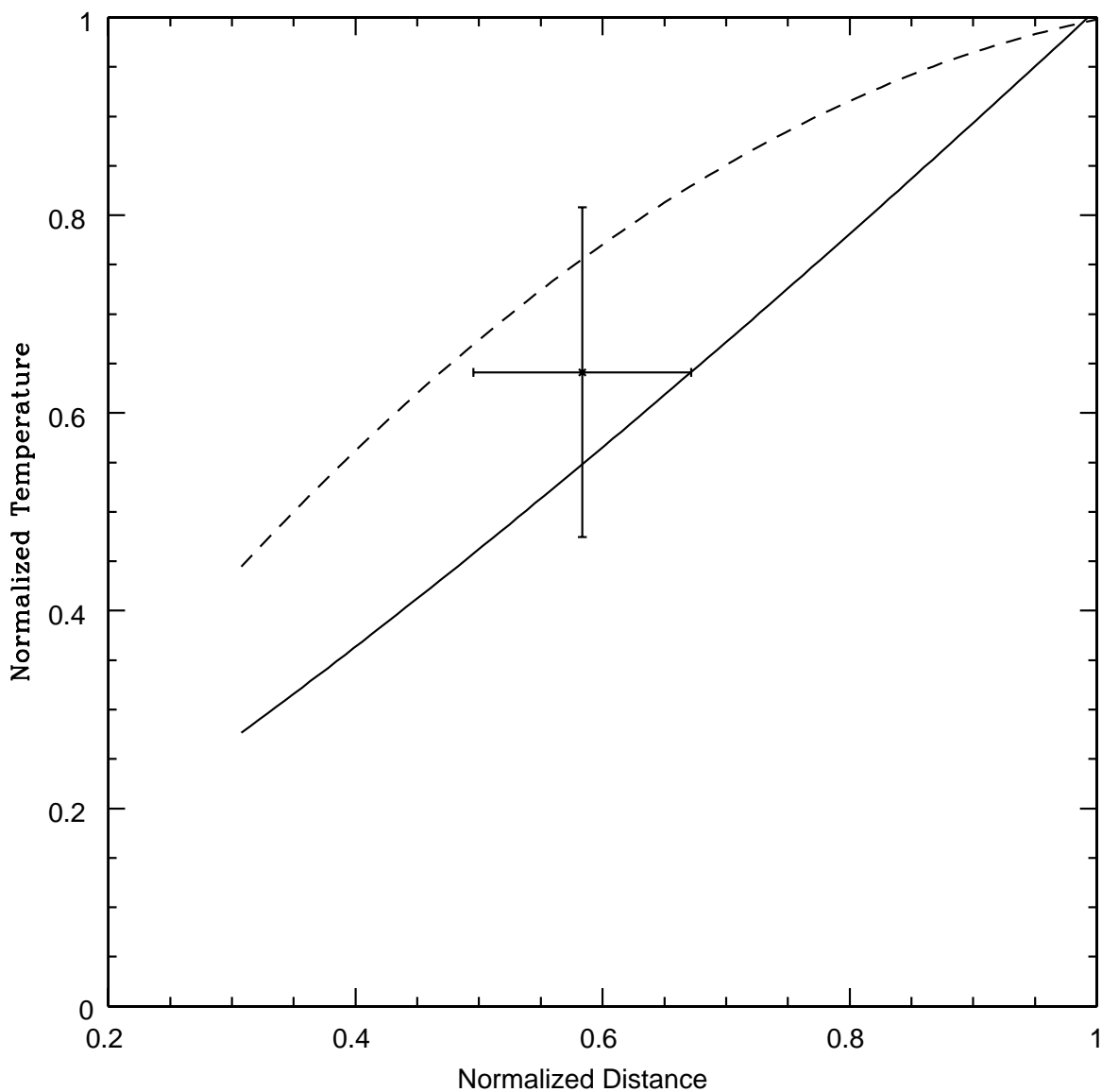


Fig. 9.— Plot of the electron temperature of the shock (normalized to the observed value at the SW boundary of the lobe) as a function of distance from the nucleus (normalized to the distance from the nucleus to the leading edge of the shock) for $M=8.3$ at the leading edge. The solid curve is the prediction based on a purely hydrodynamic model of the shock, the dashed curve from our two-fluid shock model. Thus, this plot shows the predicted variation in observed electron temperature of the shock around the periphery of the radio lobe. The point with error bars is the ratio of the observed temperatures in region 5 to region 1. The error bars on the y-axis are the 90% confidence uncertainties.

Region	Temperature (keV)	N_H (10^{21} cm $^{-2}$)	χ^2_ν
S1	0.62 ± 0.04	4.5 ± 0.6	1.5
PS1	0.23 ± 0.04	7.0 ± 1.2	1.8
S2	0.78 ± 0.06	< 2.0	0.84
PS2	0.28 ± 0.08	6.9 ± 0.2	1.3
US1	0.24 ± 0.06	3.9 ± 0.2	1.3

Table 1: Summary of best fit temperatures for regions around S1 and S2 southwest lobe shown in Figure 3. The value of N_H includes the contribution from Galactic material (8×10^{20} cm $^{-2}$). Uncertainties are 90% for one parameter of interest. See text for full description of regions.

Region	Temperature (keV)	χ^2_ν
1	$3.9^{+0.9}_{-0.7}$	0.77
1a	> 2.5	0.37
1b	$2.8^{+0.5}_{-0.4}$	0.64
1c	$3.9^{+1.1}_{-0.7}$	0.81
2	$4.4^{+2.5}_{-1.1}$	1.27
3	$3.8^{+1.4}_{-0.8}$	2.39
4	$3.1^{+0.9}_{-0.5}$	1.70
5	$2.5^{+0.6}_{-0.4}$	3.02

Table 2: Summary of best fit temperatures for regions of southwest lobe shown in Figure 4. Uncertainties are 90% for one parameter of interest. See text for full description of regions.